Equipartition of Energy Defines the Size-Thickness Relationship in Liquid-Exfoliated Nanosheets

Claudia Backes,[1*] Davide Campi,[2] Beata M. Szydlowska,[1,3] Kevin Synnatschke,[1] Ezgi Ojala,[1] Farnia Rashvand,[1] Andrew Harvey,[3] Aideen Griffin,[3] Zdenek Sofer,[4] Nicola Marzari,[2] Jonathan N. Coleman,[3*] David D. O'Regan[3*]

[1]*Chair of Applied Physical Chemistry, University of Heidelberg, Im Neuenheimer Feld 253, 69120 Heidelberg, Germany*

[2]*Theory and Simulation of Materials (THEOS) and National Centre for Computational Design and Discovery of Novel Materials (MARVEL), École Polytechnique Fédérale de Lausanne, CH-1015 Lausanne, Switzerland*

[3]*School of Physics and CRANN & AMBER Research Centers, Trinity College Dublin, The University of Dublin, Dublin 2, Ireland*

[4]*Department of Inorganic Chemistry, University of Chemistry and Technology Prague, Technická 5, 166 28 Prague 6, Czech Republic*

* backes@uni-heidelberg.de ; colemaj@tcd.ie ; david.o.regan@tcd.ie

ABSTRACT: Liquid phase exfoliation (LPE) is a commonly-used method to produce 2D nanosheets from a range of layered crystals. However, such nanosheets display broad size and thickness distributions and correlations between area and thickness, issues which limit nanosheet application-potential. To understand the factors controlling the exfoliation process, we have liquid-exfoliated 11 different layered materials, size-selecting each into fractions before using AFM to measure the nanosheet length, width and thickness distributions for each fraction. The resultant data shows a clear power-law scaling of nanosheet area with thickness for each material. We have developed a simple non-equilibrium thermodynamics-based model predicting that the power-law pre-factor is proportional to both the ratios of in-plane-tearing/out-of-plane-peeling energies and in-plane/out-of-plane moduli. By comparing the experimental data with the modulus ratio calculated from first principles, we find close agreement between experiment and theory. This supports our hypothesis that energy equipartition holds between nanosheet tearing and peeling during sonication-assisted exfoliation.

KEYWORDS: Exfoliation, 2D, size-selection, modelling, mechanics, energetics

Two-dimensional (2D) materials are a diverse family of nanostructures consisting of chemically bonded 2D monolayers that are often arranged in van der Waals-bonded few-layer stacks.[1-4] They are interesting in their own right for fundamental studies and useful in a broad range of applications.[4-6] Importantly, almost all 2D materials have physical and chemical properties that depend on the number of layers in a stack.[7] This makes control of stack (*i.e.* nanosheet) thickness important.

2D materials can be fabricated by various top-down and bottom-up techniques.[7] One important top-down technique is liquid phase exfoliation (LPE).[8, 9] This method converts 3D layered crystals into large numbers of few-layer 2D nanosheets by using an energy input to remove nanosheets from their parent crystal in a liquid environment. Due to its simplicity, scalability and compatibility with solution processing, LPE has recently gained increasing attention. Importantly, this technique is applicable to a whole host of van der Waals crystals with dozens of 2D materials having been produced in this way. A range of methods[10, 11] for inputting energy have been described, including ultrasonication[12] or shear exfoliation in rotor stator mixers,[13] kitchen blenders,[14, 15] microfluidizers,[16, 17] *via* compressive flow[18] *etc*. Overall, sonication is still the most widely used technique at the laboratory scale.

However, a significant disadvantage of LPE is that it always yields broad nanosheet size and thickness distributions,[19] rendering a precise characterisation of exfoliated nanosheets challenging and making it hard to assess exfoliation quality. This also limits the suitability of LPE nanosheets for applications.

In order to further develop LPE and to identify its intrinsic limitations as well as future opportunities, it will be essential to develop a general understanding of the fundamental physics of the exfoliation procedure. Such an understanding must be based on a broad combination of experimental data and theoretical modelling.

Here we perform a comparative study using sonication-assisted LPE to exfoliate a range of van der Waals crystals under comparable conditions. By performing extensive AFM analysis, we demonstrate a fundamental relationship between nanosheet size and thickness, which is not affected by solvent choice or sonication conditions. The existence of such a relationship allows us to propose an experimental metric for exfoliation quality. These experimental observations are underpinned by a minimal theoretical model based on the thermodynamic principle of equipartition, which results in a simple analytical relationship between nanosheet area and thickness. This model very closely describes the experimental data and links the exfoliation-

quality metric to energetic parameters associated with the breaking of both chemical and van der Waals bonds during the exfoliation process.

RESULTS AND DISCUSSION:

Size-selection and AFM analysis of nanosheets

LPE yields stock dispersions with broad lateral size and thickness distributions (see Figure 1A and SI, Figure S1). For technical reasons, this polydispersity makes statistical atomic force microscopy (AFM) characterisation challenging. As a result, we generally performed size selection of all stock dispersions by liquid cascade centrifugation (LCC), as introduced elsewhere.[19] In this iterative centrifugation process, size-selected fractions are produced in a two-step process with a low-centrifugation-rate step removing large nanosheets and a higher-centrifugation-rate step removing small nanosheets. A number of such two-step processes can be connected in a cascade to result in a set of fractions, each labelled *via* the midpoint of the centrifugation rates. This procedure yields fractions with reasonably narrow size and thickness distributions. The final supernatant obtained after the end of the cascade contains very small nanosheets (<20 nm long) and was discarded due to difficulties in accurately measuring nanosheet sizes at small lengthscales.

The size-selected fractions were deposited onto Si/SiO_2 and then subjected to size/thickness quantification by atomic force microscopy (AFM). The contrast of nanosheets deposited onto opaque bilayered substrates was exploited to identify regions promising for AFM as discussed elsewhere.[20] To minimise aggregation, the substrate was heated on a hotplate to above the boiling point of the solvent. This leads to a flash evaporation as illustrated in our previous video publication.[21] From the AFM images (examples Figure 1, for all data see SI), it is clear that the dispersed objects are 2-dimensional with lateral sizes and thicknesses that vary across fractions. For example, Figure 1 shows representative images of an unselected stock dispersion of graphite exfoliated in aqueous sodium cholate by tip sonication (Figure 1A) and images of the fractions after LCC (Figure 1B-F).

From such images, we measured the longest lateral dimension (L), the dimension perpendicular to L (the width, W) and the nanosheet thickness. This was done by manually cropping widefield images into smaller regions with only a few objects in each image and manually drawing line profiles across the nanosheets to extract the dimensions. For a visualisation see Ref [21]. Only those objects that had the distinct appearance of 2-dimensional sheets lying flat on the substrate

were counted. Other deposits such as aggregates or impurities from residual solvent or surfactant were not taken into account (examples SI Figure S3-4). By using previously established step height analysis, the apparent AFM thickness was converted to nanosheet layer number, N.[13, 19, 22-27] The resultant data can be used to calculate a number of statistical parameters such as arithmetic means: $\langle L \rangle$, $\langle W \rangle$ and $\langle N \rangle$. Example histograms are presented in Figure 2 for the fractions containing the largest (L-Gra) and the smallest (S-Gra) nanosheets produced in this particular cascade.

Comparison of graphite exfoliated under different conditions

Before investigating nanosheet exfoliation for various materials, it is first important to understand the impact of exfoliation conditions on the resultant nanosheets. To this end, graphite was exfoliated by tip sonication in aqueous sodium cholate (SC) and *N*-methyl-2-pyrrolidone (NMP) and in SC by bath sonication. One would expect the various conditions to produce nanosheet dispersions that are distinct, *i.e.* with different yield and of different nanosheet dimensions. However, a detailed comparison of statistically measured size and thickness distributions under such circumstances has not yet been reported. In all three cases, size selection by LCC was performed as explained above and the fractions were subjected to statistical AFM analysis (distribution histograms see SI Figure S6-S8). The aqueous dispersions were centrifuged for 2 h in each step, while for NMP-based dispersions the centrifugation time was 3.5 h to somewhat balance the effect of higher viscosity.

While size selection is required to make the statistical analysis of the nanosheet dimensions more feasible, it is not clear whether the resultant lateral sizes and thicknesses in the fractions are representative of the nanosheet population in the stock dispersion. In liquid cascade centrifugation, to a first approximation, the sample is fractionated by hydrodynamic volume. One may argue that the correlation between nanosheet lateral dimension and layer number typically observed[19] is thus a result of the centrifugation. However, this is not necessarily the case. As we will show below, such a correlation is present before size selection and is a consequence of the details of the exfoliation process. The fact that larger flakes tend to be thicker reflects the fact that it costs more energy to exfoliate larger-area nanosheets of a given thickness compared to smaller ones. Due to the difficulties of directly measuring nanosheet area by AFM for relative small nanosheets such as these, we use $L \times W$ as a proxy for nanosheet face area. Figure 3A shows a scatter plot of LW as function of layer number, N, of the nanosheets in the stock dispersion produced from graphite. Here, each data point represents a single nanosheet. It is clear from this plot that larger area nanosheets tend to be thicker and smaller

nanosheets tend to be thinner. Exactly the same picture is obtained when combining the data from the analysis of the fractions of the same sample after LCC (Figure 3B). This demonstrates that the distribution of nanosheet sizes in the fractions after size selection is a consequence of that in the stock. For a more detailed discussion see SI Figure S2.

Broadly similar data point clouds were obtained for the sample exfoliated in SC using a sonic bath and in NMP exfoliated with a sonic tip (Figure 3C-D). Representative widefield AFM images are shown in Figure S3-4. However, some differences can be observed: the correlation between area and layer number is softened in the case of the graphite exfoliated using SC in the bath (Figure 3C) and more large monolayers are produced at relatively low centrifugal acceleration compared to graphite exfoliated in SC with the sonic tip. In contrast, for the tip exfoliation in NMP, the area-layer number correlation is even more well-defined (Figure 3D). In addition, the data cloud is shifted toward larger/thicker nanosheets with hardly any monolayers observed. Unlike the SC-based samples, no few-layer graphene could be isolated at centrifugal accelerations higher than 6,000 *g* which suggests that fewer small/thin nanosheets are produced in NMP compared to exfoliation in aqueous surfactant. The reason for this is currently unclear, but it might be related to differences in interfacial stress transfer at solvent-nanosheet *versus* surfactant-nanosheet interfaces. However, in spite of these differences, the area-layer number data clouds seem to be centred around a similar mean area-layer number relationship as will be discussed further below.

The observation that nanosheets were isolated above 6,000 *g* in SC, but not in NMP suggests that the sonication conditions have an impact on the relative population of nanosheets in a certain size window as one would expect. This can be illustrated clearly when determining the yield (*i.e.* fraction of graphite mass converted to graphene) of nanosheets in each fraction (see methods). In all cases, the yield decreases with increasing centrifugal acceleration (Figure 3E). However, for tip-sonication the yield decreases much more steeply for NMP compared to SC, illustrating that relatively few small/thin nanosheets are produced in NMP. The overall yield summed over the fractions isolated above 100 *g* is 19.5% for the exfoliation by tip sonication in SC, only 0.3% for bath sonication in SC and 5% for tip sonication in NMP. This emphasizes that bath sonication is not suitable to produce large masses and that exfoliation in aqueous surfactant gives the best yield of few-layered material.

The overall greater population of larger/thicker nanosheets in NMP also has an impact on the mean lateral size and layer number isolated in the cascade. This is shown by the plots of mean area (expressed as $\langle LW \rangle$) and $\langle N \rangle$ as functions of the midpoint of the pair of centrifugal

accelerations used in the cascade in Figure 3F-G. The NMP data sits consistently above the SC data for both area and layer number and is also characterised by a different power law exponent relating the dimensions to RCF. Interestingly, the nanosheets produced and isolated in SC in tip and bath sonication are on average very similar, even though larger monolayers and bilayers can be produced in the bath as shown by the data cloud in Figure 3C. However, since the nanosheets in NMP are larger, but also thicker, it is important to analyse whether the relationship between $\langle LW \rangle$ and $\langle N \rangle$ varies across the samples. As mentioned above, the data clouds in Figure 3B-D seem to be centred around similar averages. To test this, we plot $\langle LW \rangle$ as function of $\langle N \rangle$ in Figure 3H. As expected from Figure 3F-G, the samples obtained by bath and tip sonication in SC fall on the same curve. However, the data for graphite exfoliated in NMP by tip sonication is shifted to higher values of $\langle LW \rangle$ and $\langle N \rangle$ and slightly offset. In all cases, $\langle LW \rangle$ is related to $\langle N \rangle$ by a powerlaw. Empirical fitting shows that the powerlaw exponent of the NMP samples is slightly different to the exponent of the samples exfoliated in SC. Interestingly, all curves project to the same value of $\langle LW \rangle$ at $\langle N \rangle = 1$. This is intriguing, as it would suggest that the (extrapolated) average size of the monolayer is identical in all cases and thus independent on the exfoliation conditions. The same behaviour is observed for WS_2 (Figure S5). One could therefore consider this value to be an interesting descriptor to evaluate the exfoliation quality across different materials. This concept will be discussed in detail below. Thus to summarise this section, while exfoliation yield, *i.e.* quantity depends strongly on sonication conditions (*e.g.* environment, power), nanosheet aspect ratios depend much more weakly on exfoliation conditions.

Materials comparison

In order to compare liquid exfoliation among various materials, we selected 11 layered van der Waals crystals with a range of structures, chemical compositions, crystallite shapes and inter- and intra-layer bonding strengths: graphite, four transition metal dichalcogenides (WS_2, MoS_2, $MoSe_2$, $PtSe_2$), hexagonal boron nitride, a post-transition metal chalcogenide with metal-metal bonds (GaS, which is interpreted here as layered Ga_2S_2), a complex layered silicate (talc) and three layered hydroxides ($Mg(OH)_2$, $Ni(OH)_2$, and $Co(OH)_2$). In most cases, liquid phase exfoliation by sonication has previously been demonstrated and yields dispersions of nanosheets with unaltered chemical composition.[13, 19, 22-28] Here, in all cases but GaS, the crystals were exfoliated in aqueous sodium cholate by tip sonication according to established

procedures (see methods). Since GaS is prone to oxidation, it was exfoliated in the solvent NMP using bath sonication.[23]

For each material, we isolated 4-6 size-selected fractions by LCC. In a few cases (WS_2, MoS_2), the size selection and centrifugation procedure was repeated under slightly varying conditions to confirm the robustness of the approach. Nanosheet dimensions were determined by AFM statistics in all cases as described above (SI, Figures S6-22). The scaling of mean nanosheet dimensions ($\langle L \rangle$, $\langle W \rangle$, $\langle N \rangle$) with central acceleration (the midpoint of the pair of centrifugal accelerations used during preparation of each fraction) is shown in Figure 4 for representative materials (for all data see Figure S23-29). It is clear that nanosheet length ($\langle L \rangle$, Figure 4A), width ($\langle W \rangle$, Figure 4B) and layer number ($\langle N \rangle$, Figure 4C) decrease as power laws with increasing centrifugal acceleration in all cases. This also implies that nanosheet dimensions (including monolayer content) scale with each other, as shown in the SI (Figure S30). Figure 4 demonstrates that, depending on the material, different lateral dimensions and layer numbers are accessible. Since the mean dimensions of the nanosheets in the fractions reflect the population in the stock dispersions, this means that sonication produces nanosheets of different length-scales and layer numbers, depending on the material. For example, the lateral dimensions of GaS are only slightly smaller than those of graphene (*i.e.*, the data points of graphene and GaS in Figure 4A and 4B sit relatively close together), but the nanosheets are significantly thicker (Figure 4C). In contrast, the WS_2 nanosheets isolated in the fractions are significantly smaller than graphene (Figure 4A and 4B), but have a comparable thickness (Figure 4C).

The data shown in Figure 4 (see also SI Figure S30) implies that the correlation between the thickness and lateral size observed for liquid-exfoliated graphene applies to a wide range of nanosheet types. To show this, we calculate $\langle LW \rangle$ and $\langle N \rangle$ for each fraction as plotted for all 11 materials in Figure 5A (and in the SI, Figure S31). In all cases, $\langle LW \rangle$ clearly scales with $\langle N \rangle$, with data from within the same class of materials (*e.g.* TMDs, hydroxides) sitting close beside each other (see also SI, Figure S32). Interestingly, there is a different offset in the data for the different material classes. This means that, depending on the material in question, the lateral dimensions achievable by sonication-based LPE for a given thickness vary significantly. For example, graphene nanosheets with a mean area <LW> of 0.01 μm^2 are 2-3 layers thick on average, while the hydroxides with similar areas have a mean layer number of 20-25. Thus, the $\langle LW \rangle$ vs $\langle N \rangle$ data allows us to quantify the exfoliation quality for a given material.

To do this, we note that, in all materials, we can nicely fit an empirical power-law scaling of $\langle LW \rangle$ with $\langle N \rangle$ (SI, Figure S31), which we write as:

$$\langle LW \rangle = D_{ML}^2 \langle N \rangle^{\beta} \quad (1)$$

Here, D_{ML} represents the characteristic lateral nanosheet size associated with monolayers (*i.e.*, when $<N>=1$) and is a measure of exfoliation quality (high D_{ML} is consistent with larger, thinner nanosheets). From fitting the data in Figure 5A, we find β to lie in the range 2-3 while D_{ML} tends to fall between ~0.5 and ~40 nm (Figure 5B).

One would naturally expect the experimentally-observed exfoliation quality (*i.e.* represented by D_{ML}) to reflect the strength of the interlayer binding energy. To test this, we have computed from quantum-mechanical first principles the inter-layer binding energy [eV/A^2], E_S, from the difference between the ground-state total energy of the optimized 3D bulk structure and that of its isolated monolayers.[29] In Figure 5B, we plot D_{ML} *versus* E_S, finding a reasonable correlation, albeit with considerable scatter. This suggests that, while the interlayer binding energy clearly plays an important role in defining the exfoliation quality, it may not be the only contributing parameter. This is a key insight that will prove important in explaining the observed nanosheet sizes, as we will discuss.

Ultrasonication is a relatively high-energy process that is known to result in sonication-induced scission during nanosheet exfoliation.[30-32] While scission is usually considered to be an inconvenience that reduces flake size, we will demonstrate that it is a critical component in the determination of nanosheet dimensions. Indeed, in many cases, nanosheets with sizes of hundreds of nanometres are exfoliated from micron-sized layered crystallites, showing that scission must occur during the exfoliation process. This implies that the intra-layer bonding strength should also play a role in determining nanosheet size. One would expect high intra-layer bonding strength (*i.e.*, high tensile strength) to result in larger nanosheets as more energy would be required to cut them to smaller sizes. Qualitatively, this could explain the scatter in Figure 5C. For example the conjugated carbon-carbon bonds in the graphene lattice are the reason for its extraordinary material strength, which would explain why larger graphene nanosheets are obtained in spite of its inter-layer binding energies being similar to those of GaS which is known to be considerably weaker then graphene.[33]

Model development

We will next build a minimal model that will help us to understand the experimentally-observed behaviour. In what follows, we will make a series of reasonable assumptions and approximations in an effort to reduce the complexity of what is, in its full extent, a formidable problem in non-equilibrium, quantum-mechanical statistical mechanics.

We may picture liquid-phase exfoliation as a violent process occurring at the nanoscale, whereby incident shock-waves of sufficiently high energy lead to the removal of small nanosheets from large, layered crystallites.[34] The process is thus characterized by rare, irreversible events that result in the breakage of both inter-layer van der Waals bonds and intra-layer chemical bonds.[34, 35] In general, the sample undergoing liquid phase exfoliation by means of external excitation (such as sonication) may be considered to be in a quasi-steady state over a suitable period of time (insofar as significant quantities of parent crystallites remain), but it is out of thermodynamic equilibrium. This lack of equilibrium, not to mention the fact that bond-breaking at nanosheet edges is an inherently quantum-mechanical but nonetheless high-energy (compared to the average thermal energy) process, implies that we ordinarily cannot appeal to basic thermodynamic principles such as the equipartition of energy between separable degrees of freedom and, indeed, even the concept of a global temperature breaks down out of equilibrium.[36]

One way forward is to note that the hypothesis of ergodicity (simplistically, that averages over large sample numbers or long times give the same results[37]) can reasonably be applied to the aggregated degrees of freedom involved in edge tearing (for nanosheets with a given edge geometric area) and, separately, surface delamination (with a given surface geometric area). Firstly, we assume that the tearing energy, $E_{Tearing}$, required to break enough intra-layer chemical bonds to remove a nanosheet from its parent crystallite is independent of the sheet shape, and is the product of the created edge geometric area, A_E, and the energy per unit area required to create edges, E_E. Similarly, we assume that the peeling or surface delamination (exfoliation) energy, $E_{Peeling}$, is the product of the new surface area, A_S, and the energy per unit area, E_S, required to peel a sheet from its parent crystal (*i.e.*, the destruction of a weakly-bonded interface, and the creation of two exposed surfaces). Secondly, and bringing in ergodicity, we may suppose that if a sufficiently large sample is taken (over time or volume, equivalently, assuming steady-state conditions macroscopically), then all nanosheet face shapes would be represented with an equal probability.

As an aside, but one relevant to our first-principles results presented later, we argue that E_E and E_S comprise only the energies required to break in-plane chemical and out-of-plane van der

Waals bonds, respectively, including local charge and ionic reorganisation but *not* solvation effects. To see this, we note that, were the system allowed to come to equilibrium (*i.e.* sonication being switched off), transition-state theory predicts that the relevant energies are the net energy changes in going from an initial state (unexfoliated crystal) to a final state (remaining crystallite plus solvated, exfoliated nanosheets), with an energy barrier controlling the kinetics. However, in the out-of-equilibrium conditions relevant to sonication, the rare and violent events that bring the system from the initial state to the transition state are reaction-limiting. As a result, we understand E_E and E_S to be properties associated only with nanosheet mechanics. While exfoliation yields are linked to solvent-nanosheet interactions as previously reported[38] and shown above, such interactions govern the stabilisation of exfoliated nanosheets rather than the actual exfoliation process.[39] In other words, as clearly demonstrated by the direct comparison of graphite and WS_2 exfoliated in aqueous surfactant solution and NMP, the relationship between lateral size and layer number is largely independent of the medium chosen for LPE while nanosheet yield is not.

Simplifying matters further is the observation that neither tearing nor delamination may occur without the other, if the net result is to be a free flake in solution. Both processes occur simultaneously during events that deliver sufficient energy to remove a nanosheet from the parent crystal. Still assuming that the relevant energies do not explicitly depend on sheet shape, we may further suppose that the tearing and delamination energies are, on average, disbursed in a fixed ratio, a, a factor which reflects the microscopic details of the exfoliation process. This gives rise to an assumed quasi-equipartition of energies for the aggregated degrees of freedom responsible for edge tearing and surface delamination. We can express this hypothesis as

$$\left\langle E_{Peeling} \right\rangle = a \times \left\langle E_{Tearing} \right\rangle \tag{2a}$$

where $\left\langle E_{Peeling} \right\rangle$ is the average contribution to the exfoliation energy associated with peeling (or delamination) of a nanosheet from its parent crystal. Similarly, $\left\langle E_{Tearing} \right\rangle$ is the average contribution associated with the breakage of in-plane bonds during nanosheet removal. In the case of perfect equipartition, we would expect a=1.

We can express equation 2a in terms of the peeling and tearing energies, E_S and E_E, as well as nanosheet dimensions:

$$2\left\langle A_S \right\rangle E_S = 2aE_E \left\langle A_E \right\rangle / 2 \tag{2b}$$

The factor of 2 on the left hand side comes from the fact that there are two surfaces created when removing a nanosheet from the layered crystal, *i.e.* on the nanosheet and on the parent crystallite. Furthermore, we note that while some nanosheets will need to have their entire perimeter created in an exfoliation event (the case of sheets being removed from the centre of the surface of the parent crystal), others will require only a very small amount of edge to be created (for example, sections connected to the main crystal by only a thin neck). Thus, on average, approximately half of a nanosheet perimeter will be newly formed during an exfoliation event, resulting in the factor of 2 in the denominator on the right hand side. However, the equivalent amount of edge must also be formed on the parent crystal, resulting in the factor of 2 in the numerator on the right hand side.

The edge area is just the product of nanosheet perimeter, P, and thickness, h_0N, where h_0 is the monolayer thickness (the parent crystallite out-of-plane unit-cell height, or the fraction of that unit-cell height associated with a single monolayer), allowing us to write

$$\langle A_S \rangle = \frac{ah_0}{2} \frac{E_E}{E_S} \langle PN \rangle \tag{3}$$

In principle, AFM images can be analysed automatically using appropriate software[34] on a sheet-by-sheet basis to obtain $\langle A_S \rangle$ and $\langle PN \rangle$ in order to test this equation. In practice, however, for the small nanosheet sizes associated with LPE nanosheets, residual solvent and aggregated sheets make automated analysis challenging. This means that manual analysis, such as that employed in this work, results in a rather limited data set consisting of length, width and thickness data for each fraction. Within a given fraction, the L, W, and N distributions are reasonably narrow (at least compared to the stock). In order to obtain averaged nanosheet area (A_S) and perimeter (P) from length (L) and width (W) data, we approximate the nanosheets as having a single fixed shape. This approximation is necessary even though nanosheet morphology is quite diverse with a large variety of nanosheet shapes present.

Although it appears more obvious to approximate the characteristic nanosheet shape as rectangular or diamond-like, here we approximate the nanosheets as elliptical. This choice is not based on an attempt to best match the observed shapes. Rather, it is an approximation designed to simplify the mathematics of the model described below (the simplification is based on the fact that within the approximation for perimeter given below, the area of a low-aspect-ratio ellipse is proportional to the square of its perimeter. This factor allows the model to be developed without any additional assumptions. See SI section 1.9). The area of an ellipse is

given by π times the product of the semi-major and semi-minor axes. Using our notation for nanosheets, this yields

$$\langle A_S \rangle = \frac{\pi}{4} \langle LW \rangle . \quad (4)$$

Next, we must address the nanosheet perimeter *P*. For ellipses with aspect ratios sufficiently close to unity, and given the approximate nature of the ellipse assumption to begin with, it is sufficient to use a low-order approximation for the ellipse perimeter, involving the geometric mean of *L* and *W* in place of the diameter of a circle. As long as the aspect ratio of each flake is not too high, we may write

$$\langle PN \rangle = \left\langle \pi \sqrt{LW} N \right\rangle = \pi \left\langle N \sqrt{LW} \right\rangle \quad (5)$$

Combining equations 3, 4 and 5:

$$\langle LW \rangle = 2ah_0 \frac{E_E}{E_S} \left\langle N \sqrt{LW} \right\rangle \quad (6)$$

Any uniform deviation from the low-aspect ratio ellipse shape assumption for the newly-created edge, such as due to roughness, is expected to primarily be hidden in the factor *a*. In order to manipulate these multi-parameter means, we make the assumption that our *L*, *W*, and *N* distribution data are consistent with:

$$\left\langle N \sqrt{LW} \right\rangle = \sqrt{\langle LW \rangle} \langle N \rangle^b \quad (7)$$

Here, the exponent *b* is expected to be close to 1 but will depend on the details of the *LW* and *N* distributions. As shown in Figure S33-34 (SI), this expression applies well to the materials studied, with values of *b* found to be mostly close to 1 and always <1.5. It is worth emphasising here that the factor <N> in this work is that of size selected fractions (see Figure S2). In principle, we can envisage no reason why our expressions should not remain valid if the nanosheets are fractionated in a different way.

Equation 7 allows us to simplify and re-cast equation 6 into the convenient form

$$\langle LW \rangle = \left(2ah_0 \frac{E_E}{E_S} \right)^2 \langle N \rangle^{2b} \quad (8)$$

This equation gives a theoretical expression for the relationship between nanosheet area (represented by $\langle LW \rangle$) and thickness (represented by $\langle N \rangle$). Importantly, it has the same form

as the empirical expression used to fit the experimental data in Figure 5A (equation 1). The fit quality shows equation 8 to be consistent with experiments across a diverse spectrum of chemical species and bonding types. We note that, while the observed power-law dependence of $\langle LW \rangle$ on $\langle N \rangle$ cannot conclusively prove the validity of our quasi-equipartition hypothesis, it strongly supports it. Indeed, it seems difficult to envisage how such a power law could come about given an absence of systematic exfoliation-energy partitioning.

Comparing model and experiment

Assuming this model does indeed describe the data, then equation 8 should be equivalent to the empirical relationship represented by equation 1. Comparing equations 1 and 8 shows that $\beta=2b$ and:

$$\frac{D_{ML}}{h_0} = 2a\frac{E_E}{E_S} \tag{9}$$

We first address the relationship between exponents. The β-exponents can be extracted by fitting the data in Figure 5A using equation 1 and are given in Figure 5B. The b-exponents can be found by fitting the statistical nanosheet size data using equation 7 as shown in Figure S33. Any systematic non-constancy of the equipartition factor a in the form of a power-law dependence on <N> will inevitably be hidden in the exponent b. As shown in Figure S34 however, the data is reasonably close to $\beta=2b$, in line with our model.

Equation 9 is very interesting, as it allows us to test the validity of our model by plotting D_{ML}/h_0 *versus* E_E/E_S. Here, D_{ML} is obtained from fitting experimental data (such as Figure 5A) while h_0 is the interlayer distance obtained from published crystallographic lattice constants (see SI, table S2) and checked for consistency against first-principles density-functional theory calculations (see SI, section 3), which agree very well. In contrast, although neither E_E or E_S are readily available for all materials, both values (or their proxies) can be computed in various ways. Assuming that data reflecting E_E/E_S were available for a range of materials, a straight-line relationship between D_{ML}/h_0 and E_E/E_S would strongly support our model and allow for the estimation of a.

To test this model, the E_S values described above (the interlayer binding energy) should be combined with an estimated in-plane bonding energy (E_E) for each material to obtain a proxy of E_E/E_S. One of the most computationally inexpensive ways to estimate E_E is by using the

integral crystal orbital Hamiltonian population (ICOHP) based on a Kohn-Sham Hamiltonian of approximate density-functional theory.[40] Shown in Figure 5D is a plot of D_{ML} / h_0 *versus* $E_{E,ICOHP} / E_S$. We find reasonable linearity, albeit with some scatter. Fitting the data to equation 9 gives a value of a=0.8±0.1.

However, $E_{E,ICOHP}$ is expected to be a crude approximation for E_E. It would be useful to have a proxy for E_E / E_S which can be calculated to a reasonable degree of accuracy. Very recently, Ji *et al.* proposed, on empirical grounds, that exfoliation quality scales with the ratio of the in-plane to out-of-plane Young's moduli of the layered material: $Y_{In-plane} / Y_{Out-of-plane}$.[41] Here, more rigorously, we develop a simple model to demonstrate that E_E / E_S and $Y_{In-plane} / Y_{Out-of-plane}$ are in fact approximately equal.

To achieve this (see SI section 4), we model the dependence of the out-of-plane interlayer interaction energy (E_{OOP}) on the inter-layer distance, r_{IL}, using a Lennard-Jones-like potential with exponents *m* and *n*:

$$E_{OOP}(r_{IL}) = \varepsilon_{vdW}\left[\frac{n}{m-n}\left(\frac{r_{vdW}}{r_{IL}}\right)^m - \frac{m}{m-n}\left(\frac{r_{vdW}}{r_{IL}}\right)^n\right] \quad (10a)$$

where r_{vdW} is the equilibrium inter-layer separation and ε_{vdW} is the binding curve well depth. Furthermore, we model the in-plane bond energy, E_{IP}, *versus* inter-atomic separation, r_{IA}, using a similar function

$$E_{IP}(r_{IA}) = \varepsilon_{bond}\left[\frac{\nu}{\mu-\nu}\left(\frac{r_{bond}}{r_{IA}}\right)^\mu - \frac{\mu}{\mu-\nu}\left(\frac{r_{bond}}{r_{IA}}\right)^\nu\right] \quad (10b)$$

Here r_{bond} is the equilibrium inter-atomic separation and ε_{bond} is the binding curve well depth. We justify using this function by noting that it is very similar in shape to the well-known Morse potential which is widely used to model bond potentials.[42] By calculating the associated spring constants from the second derivatives of the equations 10a and 10b, it is possible to show that (see SI section 4):

$$\frac{Y_{In-plane}}{Y_{Out-of-plane}} \approx \frac{\mu\nu r_{vdW}}{mn r_{bond}} \frac{E_E}{E_S} \quad (11)$$

As shown in the SI (section 4), by fitting DFT energy *versus* bond length data, we argue that, at least for graphene, $\mu\nu / r_{bond} \approx mn / r_{vdW}$, meaning that $Y_{In-plane} / Y_{Out-of-plane} \approx E_E / E_S$.

The combination of equations 9 and 11 show that we would expect D_{ML}/h_0 to scale linearly with $Y_{In-plane}/Y_{Out-of-plane}$. To test this, the in-plane and out-of-plane moduli were calculated from first principles, as detailed in the methods section. Briefly, the in-plane Young's modulus for each material was estimated from its calculated elastic coefficients c_{ij} using the formula

$$Y_{In\text{-}plane} = (c_{11}c_{22} - c_{12}c_{12})/\sqrt{c_{11}c_{22}} \quad (12)$$

that results from applying symmetry considerations to the two-dimensional Reuss average as discussed in detail in Ref. [43] and its supplemental information. This modulus is more generally computed as the inverse of the average of the compliance over in-plane angles. It assumes uniform stress rather than uniform strain conditions, as is more appropriate to the simulation of exfoliation. The coupling between the in-plane and out-of-plane degrees of freedom is neglected, *i.e.*, elements such as c_{13}. For all but the case of talc, where the above formula is a numerically small approximation, we have $c_{11} = c_{22}$ and $c_{66} = (c_{11} - c_{22})/2$ and the in-plane compliance becomes isotropic. This simple formula then recovers the two-dimensional Reuss Young's modulus exactly. The corresponding out-of-plane modulus is simply the out-of-plane elastic coefficient, $Y_{Out\text{-}of\text{-}plane} = c_{33}$. This allows us to apply the approximation that

$$\frac{E_E}{E_S} \approx \frac{Y_{In-plane}}{Y_{Out-of-plane}} = \frac{(c_{11}c_{22} - c_{12}c_{12})}{c_{33}\sqrt{c_{11}c_{22}}} \quad (13)$$

We note that $Y_{In-plane}/Y_{Out-of-plane}$ falls below 1 for the transition-metal hydroxides due to their anomalously high two-dimensional Poisson's ratio (~85% surface area conservation is predicted, assuming uniform in-plane stress).

In Figure 4D, we plot D_{ML}/h_0 *versus* $Y_{In-plane}/Y_{Out-of-plane}$, finding clear linearity and much less scatter than in Figure 5C. Assuming that $\mu\nu/r_{bond} \approx mn/r_{vdW}$ holds generally such that $Y_{In-plane}/Y_{Out-of-plane} \approx E_E/E_S$ can be applied to all data, fitting yields a value of a=1.0±0.1. As outlined above, *a*=1 is the hallmark of equipartition of energy between peeling and tearing during the exfoliation process.

The observation that our combined experimental data and theoretical modelling gives *a*-values that are reasonably close to 1 is an important result which may begin to shed light on the details of the exfoliation mechanism. However, it should be noted that there is some scope for uncertainty here due to possible cancellation of errors associated with factors such as: the

assumption that the nanosheets resemble low-aspect ellipses on average; the numerous assumptions invoked in using ICOHP or the in-and-out-of-plane Young's moduli; and the assumption of negligible <*N*>-dependence in *a* and indeed in the energies and their derivatives (which we have calculated always in the bulk limit). Nevertheless, taken together our results provide strong evidence supporting our hypothesis that quasi-equipartition holds, particularly as it explains the observed power law of equation 1.

Finally, it is interesting to note that equation 8 can be rearranged to reflect the lateral size/thickness aspect ratio, *k*, of arbitrarily thick nanosheets:

$$k = \frac{\sqrt{\langle LW \rangle}}{\langle N \rangle h_0} = 2a \frac{E_E}{E_S} \langle N \rangle^{b-1} \qquad (14)$$

Assuming that $a \approx 1$ and in the ideal case $b=1$, we find that *k* loses its <*N*>-dependence and becomes $k \approx 2E_E / E_S$, so that this is a quantity set by fundamental material parameters. This is an important result that suggests fundamental limitations of LPE nanosheets produced by means of sonication for applications such as mechanics, where high aspect ratios are important.

CONCLUSIONS

In summary, we have measured the length, width and thickness distributions of 12 different liquid-exfoliated 2D materials. We have found clear correlations between nanosheet area and thickness, allowing us to propose a metric for exfoliation quality. By developing a model for nanosheet size based on non-equilibrium thermodynamics, we give a theoretical explanation for the observed scaling and link the exfoliation quality metric to the ratio of basal-plane to edge formation energies. Using a simple model we show that this energy ratio is close to the ratio of in-plane to out-of-plane nanosheet Young's moduli. By computing these moduli, we find the model to be completely consistent with the data. Comparing data with theory strongly suggests that a generalized energy equipartition holds, on average, between nanosheet tearing and peeling during sonication, providing valuable insight into the basis physics of exfoliation.

METHODS

Materials

β-Nickel hydroxide powder (>95% 283662), magnesium hydroxide (95% 310093), cobalt hydroxide (342440), zinc hydroxide (96466), talc (243604), boron nitride (255475), graphite

(332461-2.5 kg), WS_2 (C1254), MoS_2 (69860) and sodium cholate were purchased from Sigma Aldrich. Gallium sulphide was purchased from American Elements (99.999% GaS-05-P), $MoSe_2$ (13112.14) from VWR. Selenium (99.999% and ammonium hexachloroplatinate (99.99%) were obtained from STREM. Platinum sponge was prepared by thermal decomposition of ammonium hexachloroplatinate in hydrogen at 500 °C for 1 hour. De-ionized water was prepared in house, and solvents (*N*-methyl-2-pyrrolidone and 2-propanol) used were purchased with the highest available purity.

Synthesis $PtSe_2$: Platinum diselenide was prepared by direct reaction of the elements. Stoichiometric amounts of selenium and platinum sponge corresponding to 5 g of $PtSe_2$ was placed in a quartz ampoule and melt-sealed under high vacuum. The reaction mixture was heated to 1,260 °C for one hour with a heating and cooling rate of 5 °C/min.

Exfoliation

Graphite, group VI-TMD and BN dispersions were prepared by probe sonicating the powder with an initial concentration 20 gL^{-1} in an aqueous sodium cholate (SC) solution. The powder was immersed in 80 mL of aqueous surfactant solution (C_{SC}= 6g/L). The mixture was sonicated under ice-cooling in a 100 mL metal beaker by probe sonication using a solid flathead tip (Sonics VXC-500, *i.e. 500* W) for 1 h at 60 % amplitude with a pulse of 6 s on and 2 s off. During the sonication, the sonic probe was placed 1.5 cm from the bottom of the beaker. The dispersion was centrifuged in 20 mL aliquots using 50 mL vials in a Hettich Mikro 220R centrifuge equipped with a fixed-angle rotor 1016 at 2,660 *g* for 1.5 h. The supernatant was discarded and the sediment collected in 80 mL of fresh surfactant (C_{SC}= 2 gL^{-1}) and subjected to a second sonication using a solid flathead tip (Sonics VX-500) for 5 h at 60 % amplitude with a pulse of 6 s on and 2 s off. From our experience, this two-step sonication procedure yields a higher concentration of exfoliated material and removes impurities. Graphite exfoliation in *N*-methyl-2-pyrrolidone was performed under identical conditions except for the solvent.

For the hydroxides, 1.6 g of powder was pre-treated by sonicating using a sonic tip in 80 mL deionised water for 1 h. The dispersion was then centrifuged at 2,150 *g* for 1 h and decanted with the sediment being retained and dried. The pre-treated material (20 gL^{-1}) was then sonicated in 9 g/L of sodium cholate and de-ionized water solution using a flat head tip (Sonics VCX-750) with 60% amplitude and 6s on/ 2s off for 4 h under ice cooling.

The $PtSe_2$ crystal (0.5 gL^{-1}) was immersed in 35 mL of aqueous sodium cholate (SC) solution (C_{surf} = 1.7 gL^{-1}). The mixture was sonicated under cooling in a metal beaker by probe sonication using a solid horn probe tip (Sonics VX-750) for 7.5 h at 30% amplitude with a pulse of 6 s on and 4 s off.

Gallium sulfide powder (45 gL^{-1}) was sonicated in *N*-methyl-2-pyrrolidone using an ultrasonic bath (P30 H Ultrasonic from Fischer scientific). The sonication was performed for 6 h with an amplitude of 100% and a frequency of 37 kHz in 50 mL plastic centrifuge tubes. The water in the sonic bath was cooled by a water cooling system to maintain a temperature below 30°C enabled by cold water being pumped through piping which was wrapped around the interior of the bath.

For exfoliation of graphite in aqueous sodium cholate by bath sonication, two vials each containing 40 mL of dispersed bulk graphite material in SC solution (8 gL^{-1}) were positioned in hot spots of a Branson CPX3800 sonication bath. After a sonication time of 1 h for the purification step, the dispersion was centrifuged at 2,660 *g* for 1.5 h, the impurity rich supernatant discarded. The sediment was collected in fresh SC solution (2 gL^{-1}) for the second exfoliation step with a sonication time of 5 h. During the bath sonication, the bath water was replaced every 30 min with new water to avoid overheating.

Size selection

To select nanosheets by size, we used liquid cascade centrifugation with sequentially increasing rotation speeds. Centrifugation conditions are expressed as relative centrifugal force (RCF) in units of $10^3 \times g$ (or k *g*) with *g* being the gravitational force. Two different centrifuges were used: For centrifugal accelerations < 3,000 *g*, a Hettich Mikro 220R centrifuge equipped with a fixed-angle rotor 1195-A was used; above 3,000 *g*, a Beckman Coulter Avanti XP centrifuge with a JA25.50 fixed angle rotor was used. Graphite, BN, TMDs: All centrifugation runs were performed for 2 h (10°C). Unexfoliated material was removed by centrifugation at 100 *g*. The supernatant was subjected to further centrifugation at 400 *g*. The sediment was collected in fresh surfactant (C_{SC}= 0.1 gL^{-1}) at reduced volume (3-8 mL), while the supernatant was centrifuged at 1,000 *g*. Again, the sediment was collected and the supernatant subjected to centrifugation at higher speeds. This procedure was repeated with the following RCF: 5k *g*, 10k *g*, 22k *g*, 74k *g*. As sample nomenclature, the lower and upper boundary of the centrifugation are indicated. For graphite exfoliated in NMP, centrifugation was performed for 3.5 h to balance the slower sedimentation rate in the higher viscosity solvent. Since fewer small/thin nanosheets

are produced, steps with lower centrifugal acceleration were included with the following overall cascade: 30 *g*, 100 *g*, 400 *g*, 1k *g*, 3k *g*, 6k *g*.

For $PtSe_2$, centrifugation was performed for 2 h in each step. Unexfoliated material was first removed by centrifugation at 100 *g* (50 mL vial). The supernatant was than subjected to further centrifugation at 400 *g* (50 mL vial). The sediment was collected in fresh SC-H_2O (0.1 gL^{-1}), while the supernatant was centrifuged at 1,000 *g* (50 ml vial). Again, the sediment was collected, and the supernatant subjected to centrifugation at higher speeds. This procedure was repeated with the following speeds: 3k *g* (50 ml vial), 5k *g* (50 ml vial), 10k *g* (50 ml vial), 30k *g* (2x12 ml vial).

In the case of the hydroxide and talc dispersions, centrifugation parameters were adjusted: the stock obtained after sonication was centrifuged at 25 *g* for 60 min. The sediment was discarded and the supernatant was centrifuged at 100 *g* for 60 min. The sediment after this centrifugation step was redispersed in fresh surfactant solution (1 h bath sonication, c_{SC}=9 gL^{-1}) producing the largest size. The supernatant after the 100 *g* centrifugation step was centrifuged at 250 *g* for 60 min, producing the second largest size in the redispersed sediment. These steps were repeated in further increments of 400 *g*, 1k *g*, and 3k *g*, thus producing five sizes. For GaS, centrifugation was performed for 2 h in each step using 25 *g* (unexfoliated removed), 100 *g*, 400 *g*, 1k *g*, 3k *g*, 10k *g*. In this case, the sediment was redispersed in 2-propanol to facilitate deposition for AFM. The final supernatants were discarded in all cases.

Characterisation

Atomic force microscopy (AFM) was carried out on a Dimension ICON3 scanning probe microscope (Bruker AXS S.A.S.) in ScanAsyst in air under ambient conditions using aluminium coated silicon cantilevers (OLTESPA-R3). The concentrated dispersions were diluted with water (or 2-propanol in the case of GaS) to optical densities <0.1 across the resonant spectral region. A drop of the dilute dispersions (20 µL) was deposited on pre-heated (180 °C) Si/SiO_2 wafers (0.5×0.5 cm^2) with an oxide layer of 300 nm. After deposition, the wafers were rinsed with ~5 mL of water and ~5 mL of isopropanol. Typical image sizes ranged from 15×15 for larger nanosheets to 5×5 μm^2 at scan rates of 0.5-0.8 Hz with 1024 lines per image. Published values for step heights were used to convert apparent AFM thickness to layer number.[13, 19, 22-27] The step height analysis of $PtSe_2$ is shown in the SI (Figure S14). Previously published length corrections were used to correct lateral dimensions from cantilever broadening.[44] A detailed description of the statistical analysis is provided in the SI (section 5).

The yield of the exfoliation in graphite was determined as follows: Extinction spectra were measured with a known dilution factor for each fraction on a Agilent Carry 6000i (quartz cuvettes, 0.4 cm pathlength). With the size-independent extinction coefficient of 5,450 $Lg^{-1}m^{-1}$ at 750 nm, the concentration of dispersed graphite was calculated.[45] The volume of each fraction was measured to calculate the mass and thus the yield through dividing by the initial mass of graphite (2.4 g).

Calculation of binding energies

All first-principles calculations were carried out using Kohn-Sham density-functional theory as implemented the Quantum Espresso package.[46] The binding energies for non-magnetic materials has been computed in Ref. [29] using SSSP efficiency v.07 pseudopotentials[47] and suggested cut-offs, a k-point density of 0.2 A^{-1} (Ref. [27]) and a Marzari-Vanderbilt cold smearing[48] of 0.02 Ry. The vdW-DF2-C09[49-51] van der Waals functional was used. The binding energy of magnetic materials was validated using the RVV10 functional[52-54] and by performing collinear spin-polarized calculations considering the magnetic ground state of the bulk structure and each isolated substructure. Despite this, the binding energies of magnetic materials $Ni(OH)_2$ and $Co(OH)_2$ are likely to be subject to larger errors due the difficulties in accurately simulating d electrons in contemporary approximate DFT. The calculation of the integral crystal orbital Hamiltonian population (ICOHP) was performed using the Lobster code[55] post-processing calculations carried out with PAW pseudopotentials[56] from the PSlibrary set.[46] An indication of the energy per unit area required to create edges, E_E , has been obtained by summing up the ICOHP energies of the minimum number of bonds per unit cell that have to be broken in order to create the edge, divided by the layer thickness h_0. The data is summarised in SI, section 3.

Calculation of elastic constants

Elastic constants were computed by finite deformations and exploiting the stress-strain relation as implemented in the ElaStic module[57] using 9 deformed structures for each symmetry-independent strain and a maximum strain of 0.004. Both the vdW-DF2-C09 and RVV10 functionals were used for non-magnetic structures, while only RVV10 was used for magnetic materials due to the current limitations in the Quantum Espresso implementation. A refined k-point density of 0.05 A^{-1} was employed, as well as an increased cutoff (30 Ry over the SSSP v0.7 recommendation) to ensure an high accuracy stress converge for all the materials. Forces were relaxed down to 5×10^{-5} Ry/a.u., while stress has been optimized up to a threshold of 0.05 kbar within structural optimizations. The data is summarised in SI, section 3.

Acknowledgements

We acknowledge the European Union under grant agreements n°785219 Graphene Flagship-core 2. C.B. acknowledges support from the German research foundation (DFG) under grant agreement Emmy-Noether, BA4856/2-1 and Jana Zaumseil for the access to the infrastructure at the Chair of Applied Physical Chemistry. Additional support was provided by Science Foundation Ireland (SFI/12/RC/2278) and the European Research Council Advanced Grant (FUTURE-PRINT). D.C. and N.M. acknowledge support from the H2020 MaX Centre of Excellence and the MARVEL NCCR. D.C. acknowledge support from the EPFL Fellows fellowship programme co-funded by Marie Sklodowska-Curie, Horizon 2020 grant agreement no. 665667. Simulation time was awarded PRACE on Marconi at Cineca, Italy (project id. 2016163963). Z.S. was supported by the Czech Science Foundation (GACR No. 17-11456S) and by the project Advanced Functional Nanorobots (reg. No. CZ.02.1.01/0.0/0.0/15_003/0000444 financed by the EFRR).

Author contributions

C.B. designed the experiments, performed AFM and analyzed all data; D.C. and N.M. performed first-principles simulations; D.D.O'R calculated elastic moduli; B.M.S., K.S., E.O., F.R., A.H., A.G. prepared samples; B.M.S., K.S., performed AFM; Z.S. synthesized bulk $PtSe_2$; J.N.C. and D.D.O'R. developed the model, and C.B., J.N.C. and D.D.O'R wrote the manuscript.

Additional information

Supplementary information is available in the online version of the paper. Correspondence and requests for materials should be addressed to C. B., D.D.O'R, or J.N.C.

FIGURES

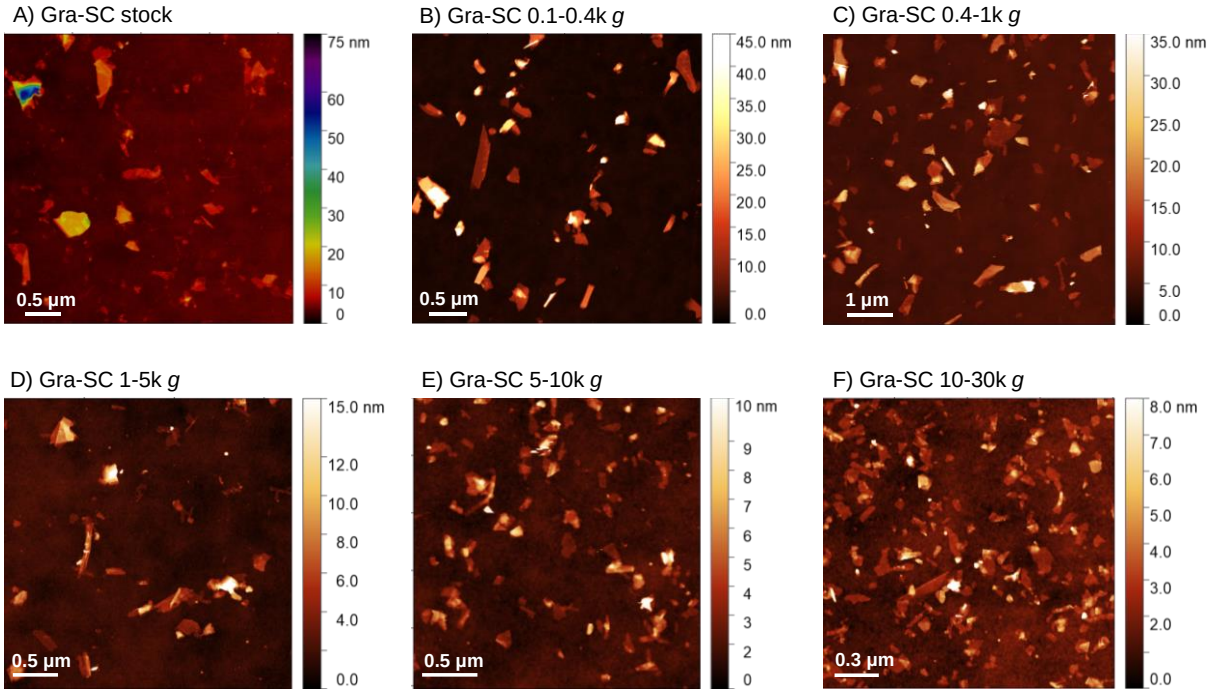

Figure 1: AFM images of graphite exfoliated in aqueous SC solution by tip sonication both before and after size selection. A) Unselected stock dispersion, B-F) fractions after liquid cascade centrifugation isolated from the stock dispersion shown in A. B) Fraction of largest nanosheets isolated by centrifugation between 100-400 *g*. C) 400-1,000 *g* fraction, D) 1-5k *g* fraction, E) 5-10k *g* fraction, F) Fraction of smallest nanosheets isolated by centrifugation between 10-30k *g*. Material remaining in the supernatant after centrifugation at 30k *g* was discarded.

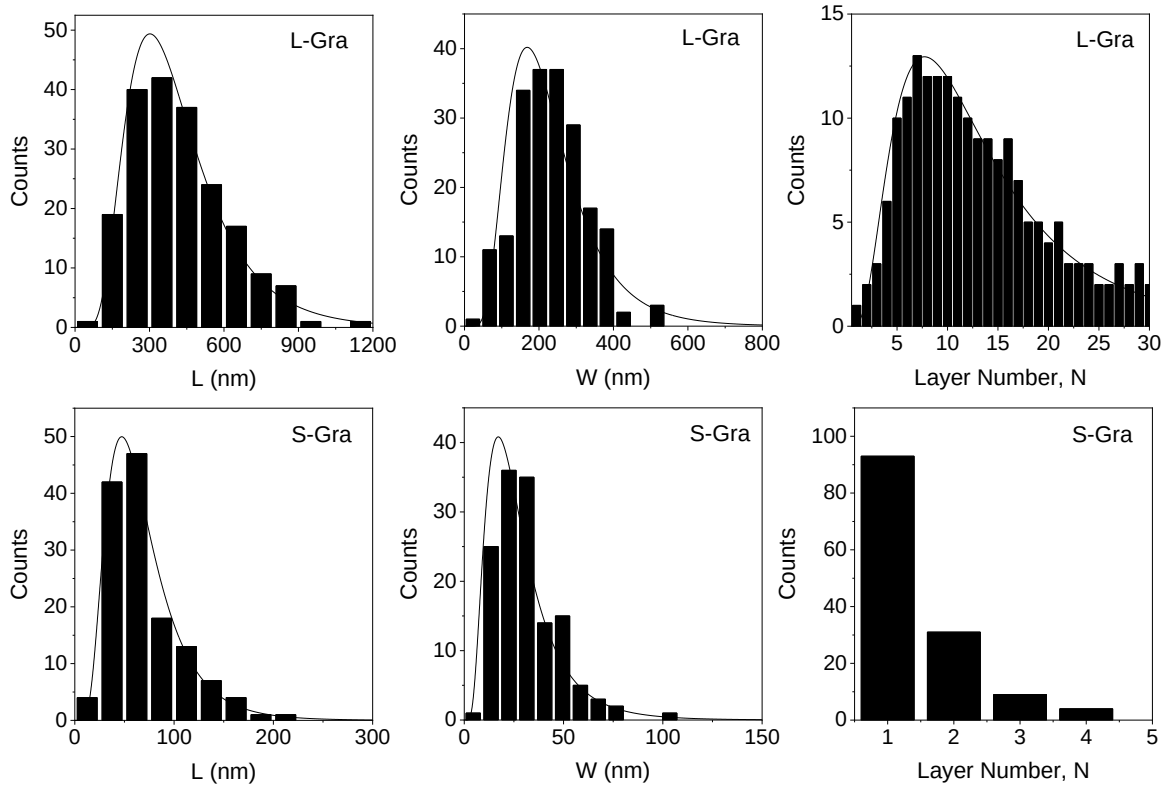

Figure 2: Size distribution histograms determined from AFM statistics. A-B) Longest lateral dimension, length L, for A) large nanosheets, B) small nanosheets. C-D) Dimension perpendicular to longest dimension, width W, for C) large nanosheets, D) small nanosheets. E-F) Nanosheet layer number, N, for E) large nanosheets, F) small nanosheets. For additional data, see SI. These particular distributions are for graphene nanosheets exfoliated in SC using a sonic tip. Large and small nanosheets were prepared using the centrifugation parameters 0.1-0.4k *g* and 10-30k *g* respectively. Solid lines are lognormal fits.

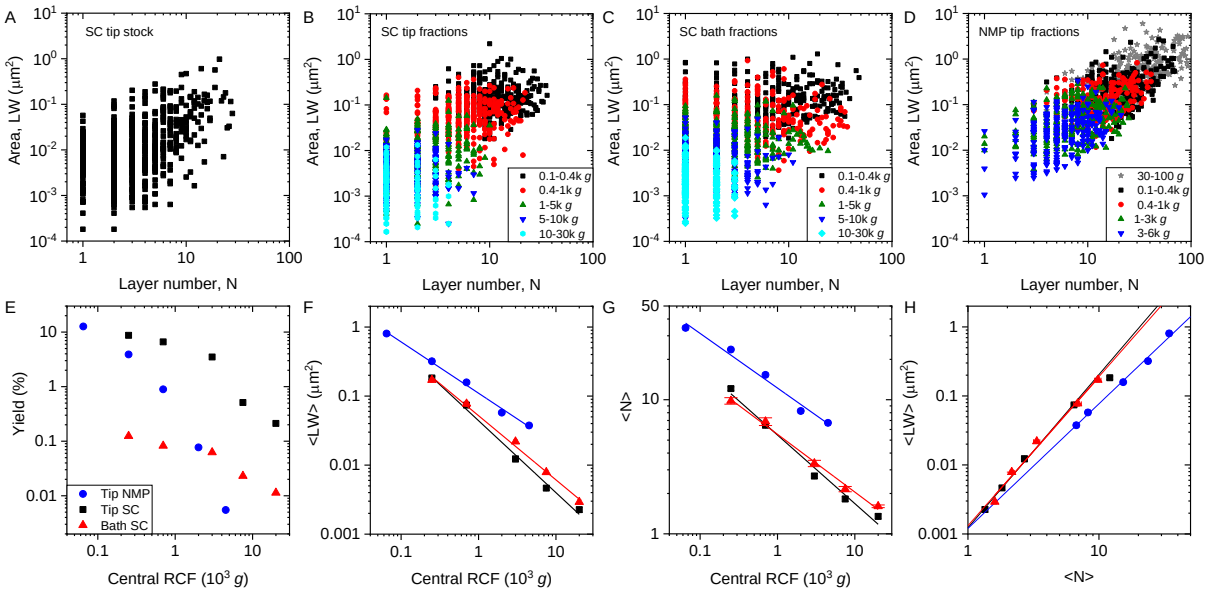

Figure 3: Size analysis of graphite exfoliated using different conditions. A-D) Scatter plots of nanosheet area (L×W) as function of layer number (N). Each data point represents an individual nanosheet. A) Stock dispersion after tip sonication in aqueous sodium cholate. B) Same sample as in (A) after size selection by liquid cascade centrifugation. The different fractions are color-coded. C) Nanosheet dimension data cloud for graphite exfoliated in aqueous sodium cholate by bath sonication. D) Nanosheet dimension data cloud for graphite exfoliated in NMP by tip sonication. E) Plot of nanosheet yield as function of midpoint of the pair of centrifugal accelerations used in the centrifugation cascade (central RCF). F) Plot of mean nanosheet area (<LW>) of the fractions as function of the central RCF. G) Plot of mean nanosheet layer number (<N>) as function of the central RCF. H) Plot of mean nanosheet area as function of layer number.

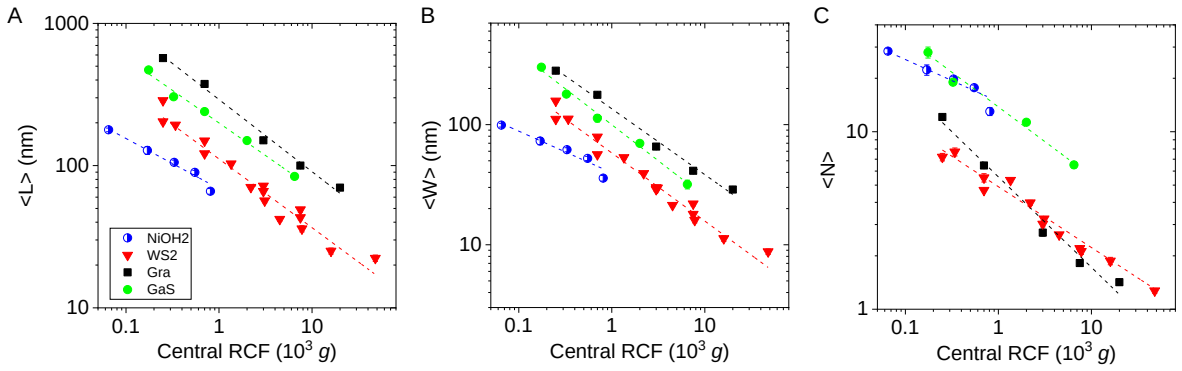

Figure 4: Scaling of nanosheet dimension with centrifugal acceleration. Plots of A) Mean nanosheet length, <*L*>, B) mean width, <*W*> and C) Mean layer number, <*N*> as function of the midpoint of the pair of centrifugal acceleration used for the size selection. Data for four representative materials under study are shown. For additional data, see SI. In all cases, the reduction in lateral dimensions and layer number with increasing centrifugal acceleration is evident. Lines are power law fits provided as guide for the eye.

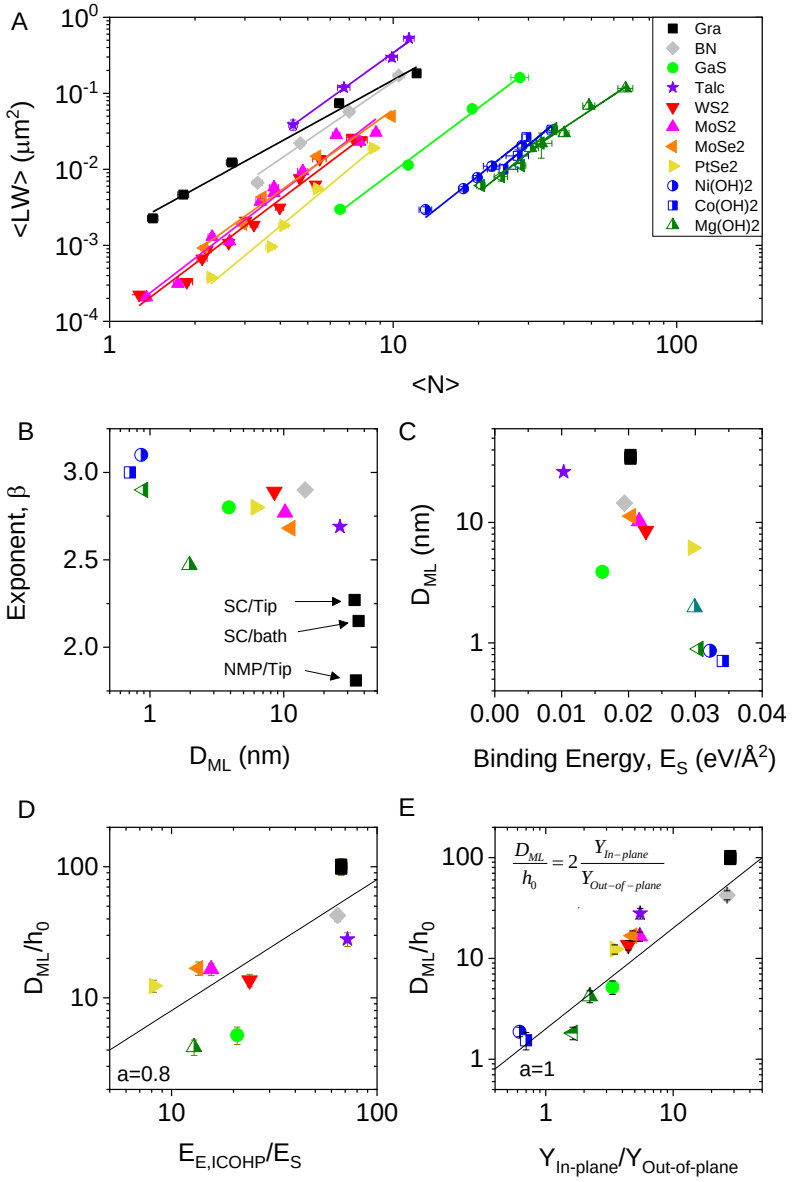

Figure 5: Evaluation of the exfoliation efficiency compared to theoretical data. A) Plot of the (experimental) mean nanosheet area approximated as the product of length and width, $\langle LW \rangle$ as function of mean layer number, $\langle N \rangle$ for all materials under study. The nanosheet area increases as a power-law with thickness as illustrated by solid lines. Extrapolation of the fit lines to $\langle N \rangle = 1$ gives a quantitative description of the exfoliation efficiency, D_{ML}^2, where D_{ML} is a characteristic lateral size associated with monolayers. Materials within the same class (transition metal dichalcogenides or hydroxides) sit very close beside each other. B) Map showing power-law fit parameters, β and D_{ML}. C) Plots of D_{ML} against calculated interlayer binding energies, E_S. D-E) Plots of D_{ML} / h_0 against parameters designed to approximate the ratio of in-plane to out-of-plane bonding strengths. In D, this ratio is represented by the ratio of the integral crystal orbital Hamiltonian population (ICOHP) surface density over the interlayer

binding energy density while in E) we use the calculated ratio of the in-plane to out-of-plane Young's moduli. The solid lines are fits to equation 9. In B-E, the three graphene data points reflect the samples prepared by sonication with both tip and bath in NMP and sodium cholate (SC).

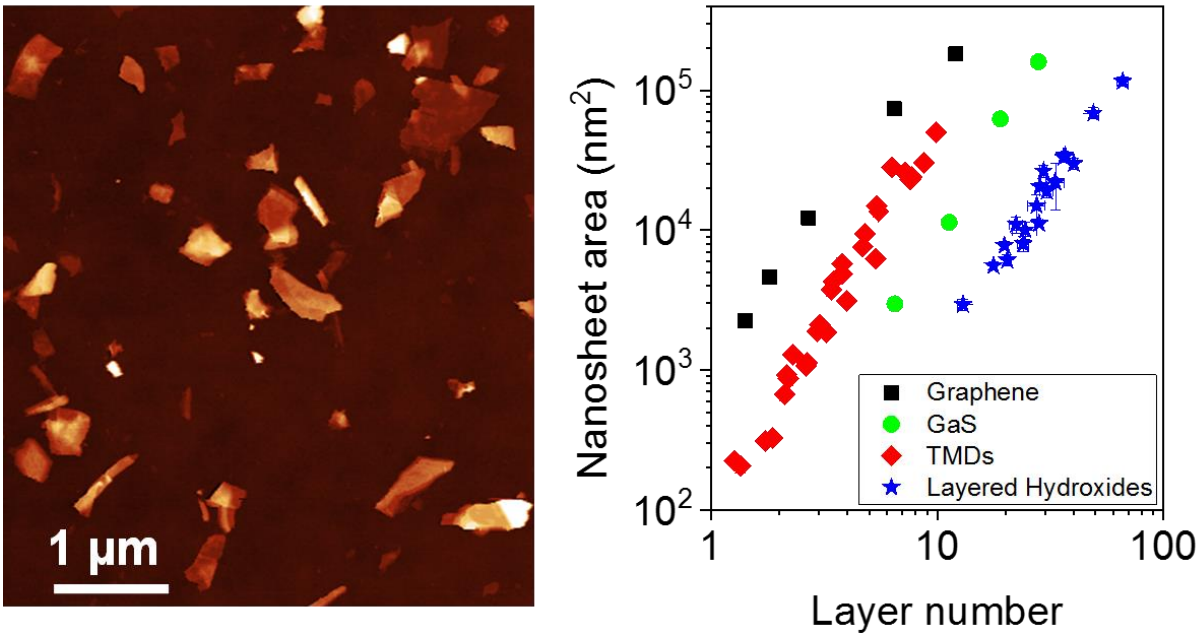

ToC fig

References

1. Chhowalla, M.; Shin, H. S.; Eda, G.; Li, L. J.; Loh, K. P.; Zhang, H., The Chemistry of Two-Dimensional Layered Transition Metal Dichalcogenide Nanosheets. *Nature Chem.* **2013,** 5, 263-275.
2. Ma, R.; Sasaki, T., Two-Dimensional Oxide and Hydroxide Nanosheets: Controllable High-Quality Exfoliation, Molecular Assembly, and Exploration of Functionality. *Acc. Chem. Res.* **2015,** 48, 136-143.
3. Jiang, S.; Arguilla, M. Q.; Cultrara, N. D.; Goldberger, J. E., Covalently-Controlled Properties by Design in Group Iv Graphane Analogues. *Acc. Chem. Res.* **2015,** 48, 144-151.
4. Anasori, B.; Lukatskaya, M. R.; Gogotsi, Y., 2d Metal Carbides and Nitrides (Mxenes) for Energy Storage. *Nat. Rev. Mater.* **2017,** 2, 16098.
5. Novoselov, K. S.; Fal'ko, V. I.; Colombo, L.; Gellert, P. R.; Schwab, M. G.; Kim, K., A Roadmap for Graphene. *Nature* **2012,** 490, 192-200.
6. Das, S.; Robinson, J. A.; Dubey, M.; Terrones, H.; Terrones, M., Beyond Graphene: Progress in Novel Two-Dimensional Materials and Van Der Waals Solids. *Annu. Rev. Mater. Res.* **2015,** 45, 1-27.
7. Wang, Q. H.; Kalantar-Zadeh, K.; Kis, A.; Coleman, J. N.; Strano, M. S., Electronics and Optoelectronics of Two-Dimensional Transition Metal Dichalcogenides. *Nat. Nanotechnol.* **2012,** 7, 699-712.
8. Bonaccorso, F.; Bartolotta, A.; Coleman, J. N.; Backes, C., 2d-Crystal-Based Functional Inks. *Adv. Mater.* **2016,** 28, 6136-6166.
9. Nicolosi, V.; Chhowalla, M.; Kanatzidis, M. G.; Strano, M. S.; Coleman, J. N., Liquid Exfoliation of Layered Materials. *Science* **2013,** 340, 1226419.

10. Yi, M.; Shen, Z., A Review on Mechanical Exfoliation for the Scalable Production of Graphene. *J. Mater. Chem. C.* **2015,** 3, 11700-11715.
11. Tao, H.; Zhang, Y.; Gao, Y.; Sun, Z.; Yan, C.; Texter, J., Scalable Exfoliation and Dispersion of Two-Dimensional Materials - an Update. *Phys. Chem. Chem. Phys.* **2017,** 19, 921-960.
12. Coleman, J. N.; Lotya, M.; O'Neill, A.; Bergin, S. D.; King, P. J.; Khan, U.; Young, K.; Gaucher, A.; De, S.; Smith, R. J.; Shvets, I. V.; Arora, S. K.; Stanton, G.; Kim, H. Y.; Lee, K.; Kim, G. T.; Duesberg, G. S.; Hallam, T.; Boland, J. J.; Wang, J. J., *et al.*, Two-Dimensional Nanosheets Produced by Liquid Exfoliation of Layered Materials. *Science* **2011,** 331, 568-571.
13. Paton, K. R.; Varrla, E.; Backes, C.; Smith, R. J.; Khan, U.; O'Neill, A.; Boland, C.; Lotya, M.; Istrate, O. M.; King, P.; Higgins, T.; Barwich, S.; May, P.; Puczkarski, P.; Ahmed, I.; Moebius, M.; Pettersson, H.; Long, E.; Coelho, J.; O'Brien, S. E., *et al.*, Scalable Production of Large Quantities of Defect-Free Few-Layer Graphene by Shear Exfoliation in Liquids. *Nat. Mater.* **2014,** 13, 624-630.
14. Varrla, E.; Paton, K. R.; Backes, C.; Harvey, A.; Smith, R. J.; McCauley, J.; Coleman, J. N., Turbulence-Assisted Shear Exfoliation of Graphene Using Household Detergent and a Kitchen Blender. *Nanoscale* **2014,** 6, 11810-11819.
15. Yi, M.; Shen, Z., Kitchen Blender for Producing High-Quality Few-Layer Graphene. *Carbon* **2014,** 78, 622-626.
16. Karagiannidis, P. G.; Hodge, S. A.; Lombardi, L.; Tomarchio, F.; Decorde, N.; Milana, S.; Goykhman, I.; Su, Y.; Mesite, S. V.; Johnstone, D. N.; Leary, R. K.; Midgley, P. A.; Pugno, N. M.; Torrisi, F.; Ferrari, A. C., Microfluidization of Graphite and Formulation of Graphene-Based Conductive Inks. *ACS Nano* **2017,** 11, 2742-2755.
17. Keith, R. P.; James, A.; Andrew, J. P.; Toby, S., Production of Few-Layer Graphene by Microfluidization. *Mater. Res. Express* **2017,** 4, 025604.
18. Rizvi, R.; Nguyen, E. P.; Kowal, M. D.; Mak, W. H.; Rasel, S.; Islam, M. A.; Abdelaal, A.; Joshi, A. S.; Zekriardehani, S.; Coleman, M. R.; Kaner, R. B., High-Throughput Continuous Production of Shear-Exfoliated 2d Layered Materials Using Compressible Flows. *Adv. Mater.* **2018,** 30, 1800200.
19. Backes, C.; Szydłowska, B. M.; Harvey, A.; Yuan, S.; Vega-Mayoral, V.; Davies, B. R.; Zhao, P.-l.; Hanlon, D.; Santos, E. J. G.; Katsnelson, M. I.; Blau, W. J.; Gadermaier, C.; Coleman, J. N., Production of Highly Monolayer Enriched Dispersions of Liquid-Exfoliated Nanosheets by Liquid Cascade Centrifugation. *ACS Nano* **2016,** 10 1589-1601.
20. Backes, C.; Higgins, T. M.; Kelly, A.; Boland, C.; Harvey, A.; Hanlon, D.; Coleman, J. N., Guidelines for Exfoliation, Characterization and Processing of Layered Materials Produced by Liquid Exfoliation. *Chem. Mater.* **2017,** 29, 243-255.
21. Backes, C.; Hanlon, D.; Szydlowska, B. M.; Harvey, A.; Smith, R. J.; Higgins, T. M.; Coleman, J. N., Preparation of Liquid-Exfoliated Transition Metal Dichalcogenide Nanosheets with Controlled Size and Thickness. *Journal of Visualised Experiments* **2016,** 118.
22. Backes, C.; Smith, R. J.; McEvoy, N.; Berner, N. C.; McCloskey, D.; Nerl, H. C.; O'Neill, A.; King, P. J.; Higgins, T.; Hanlon, D.; Scheuschner, N.; Maultzsch, J.; Houben, L.; Duesberg, G. S.; Donegan, J. F.; Nicolosi, V.; Coleman, J. N., Edge and Confinement Effects Allow *in Situ* Measurement of Size and Thickness of Liquid-Exfoliated Nanosheets. *Nature Commun.* **2014,** 5, 4576.
23. Harvey, A.; Backes, C.; Gholamvand, Z.; Hanlon, D.; McAteer, D.; Nerl, H. C.; McGuire, E.; Seral-Ascaso, A.; Ramasse, Q. M.; McEvoy, N.; Winters, S.; Berner, N. C.; McCloskey, D.; Donegan, J.; Duesberg, G.; Nicolosi, V.; Coleman, J. N., Preparation of Gallium Sulfide Nanosheets by Liquid Exfoliation and Their Application as Hydrogen Evolution Catalysts. *Chem. Mater.* **2015,** 27, 3483–3493.
24. Harvey, A.; He, X.; Godwin, I. J.; Backes, C.; McAteer, D.; Berner, N. C.; McEvoy, N.; Ferguson, A.; Shmeliov, A.; Lyons, M. E. G.; Nicolosi, V.; Duesberg, G. S.; Donegan, J. F.; Coleman, J. N., Production of Ni(Oh)2 Nanosheets by Liquid Phase Exfoliation: From Optical Properties to Electrochemical Applications. *J. Mater. Chem. C.* **2016,** 4, 11046-11059.
25. McAteer, D.; Godwin, I. J.; Ling, Z.; Harvey, A.; He, L.; Boland, C. S.; Vega-Mayoral, V.; Szydłowska, B.; Rovetta, A. A.; Backes, C.; Boland, J. B.; Chen, X.; Lyons, M. E. G.; Coleman, J. N., Liquid Exfoliated Co(Oh)2 Nanosheets as Low-Cost, yet High-Performance, Catalysts for the Oxygen Evolution Reaction. *Adv. Energy Mater.* **2018,** 8, 1702965.

26. Griffin, A.; Harvey, A.; Cunningham, B.; Scullion, D.; Tian, T.; Shih, C.-J.; Gruening, M.; Donegan, J. F.; Santos, E. J. G.; Backes, C.; Coleman, J. N., Spectroscopic Size and Thickness Metrics for Liquid-Exfoliated H-Bn. *Chem. Mater.* **2018,** 30, 1998-2005.
27. Andrew, H.; John, B. B.; Ian, G.; Adam, G. K.; Beata, M. S.; Ghulam, M.; Andrew, T.; David, J. L.; Paul, O. B.; Jonathan, N. C., Exploring the Versatility of Liquid Phase Exfoliation: Producing 2d Nanosheets from Talcum Powder, Cat Litter and Beach Sand. *2D Mater.* **2017,** 4, 025054.
28. Harvey, A.; Backes, C.; Boland, J. B.; He, X.; Griffin, A.; Szydlowska, B.; Gabbett, C.; Donegan, J. F.; Coleman, J. N., Non-Resonant Light Scattering in Dispersions of 2d Nanosheets. *Nature Commun.* **2018,** 9, 4553.
29. Mounet, N.; Gibertini, M.; Schwaller, P.; Campi, D.; Merkys, A.; Marrazzo, A.; Sohier, T.; Castelli, I. E.; Cepellotti, A.; Pizzi, G.; Marzari, N., Two-Dimensional Materials from High-Throughput Computational Exfoliation of Experimentally Known Compounds. *Nat. Nanotechnol.* **2018,** 13, 246-252.
30. Cravotto, G.; Cintas, P., Sonication-Assisted Fabrication and Post-Synthetic Modifications of Graphene-Like Materials. *Chem.: Eur. J.* **2010,** 16, 5246-5259.
31. Khan, U.; O'Neill, A.; Lotya, M.; De, S.; Coleman, J. N., High-Concentration Solvent Exfoliation of Graphene. *Small* **2010,** 6, 864-871.
32. O'Neill, A.; Khan, U.; Coleman, J. N., Preparation of High Concentration Dispersions of Exfoliated Mos2 with Increased Flake Size. *Chem. Mater.* **2012,** 24, 2414-2421.
33. Hess, P., Predictive Modeling of Intrinsic Strengths for Several Groups of Chemically Related Monolayers by a Reference Model. *Phys. Chem. Chem. Phys.* **2018,** 20, 7604-7611.
34. Liscio, A.; Kouroupis-Agalou, K.; Betriu, X. D.; Kovtun, A.; Treossi, E.; Pugno, N. M.; De Luca, G.; Giorgini, L.; Palermo, V., Evolution of the Size and Shape of 2d Nanosheets During Ultrasonic Fragmentation. *2D Mater.* **2017,** 4.
35. Xia, Z. Y.; Pezzini, S.; Treossi, E.; Giambastiani, G.; Corticelli, F.; Morandi, V.; Zanelli, A.; Bellani, V.; Palermo, V., The Exfoliation of Graphene in Liquids by Electrochemical, Chemical, and Sonication-Assisted Techniques: A Nanoscale Study. *Adv. Funct. Mater.* **2013,** 23, 4684-4693.
36. Jou, D.; Casas-Vázquez, J.; Criado-Sancho, M., *Thermodynamics of Fluids under Flow*. Springer Netherlands: Netherlands, 2011.
37. Lucia, U., Probability, Ergodicity, Irreversibility and Dynamical Systems. *Proc. R. Soc. London, A* **2008,** 464, 1089-1104.
38. Hernandez, Y.; Nicolosi, V.; Lotya, M.; Blighe, F. M.; Sun, Z. Y.; De, S.; McGovern, I. T.; Holland, B.; Byrne, M.; Gun'ko, Y. K.; Boland, J. J.; Niraj, P.; Duesberg, G.; Krishnamurthy, S.; Goodhue, R.; Hutchison, J.; Scardaci, V.; Ferrari, A. C.; Coleman, J. N., High-Yield Production of Graphene by Liquid-Phase Exfoliation of Graphite. *Nat. Nanotechnol.* **2008,** 3, 563-568.
39. Barwich, S.; Khan, U.; Coleman, J. N., A Technique to Pretreat Graphite Which Allows the Rapid Dispersion of Defect-Free Graphene in Solvents at High Concentration. *J. Phys. Chem. C* **2013,** 117, 19212-19218.
40. Dronskowski, R.; Blochl, P. E., Crystal Orbital Hamilton Populations (Cohp) - Energy-Resolved Visualization of Chemical Bonding in Solids Based on Density-Functional Calculations. *J. Phys. Chem.* **1993,** 97, 8617-8624.
41. Ji, L. J.; Qin, Y.; Gui, D.; Li, W.; Li, Y. C.; Li, X. D.; Lu, P. X., Quantifying the Exfoliation Ease Level of 2d Materials *Via* Mechanical Anisotropy. *Chem. Mater.* **2018,** 30, 8732-8738.
42. Kalosakas, G.; Lathiotakis, N. N.; Galiotis, C.; Papagelis, K., In-Plane Force Fields and Elastic Properties of Graphene. *J. Appl. Phys.* **2013,** 113, 7.
43. Moynihan, G.; Sanvito, S.; O'Regan, D. D., Strain-Induced Weyl and Dirac States and Direct-Indirect Gap Transitions in Group-V Materials. *2D Mater.* **2017,** 4.
44. Ueberricke, L.; Coleman, J. N.; Backes, C., Robustness of Size Selection and Spectroscopic Size, Thickness and Monolayer Metrics of Liquid-Exfoliated Ws2. *Phys. Status Solidi B* **2017,** 254, 1700443.
45. Backes, C.; Paton, K. R.; Hanlon, D.; Yuan, S.; Katsnelson, M. I.; Houston, J.; Smith, R. J.; McCloskey, D.; Donegan, J. F.; Coleman, J. N., Spectroscopic Metrics Allow *in Situ* Measurement of Mean Size and Thickness of Liquid-Exfoliated Few-Layer Graphene Nanosheets. *Nanoscale* **2016,** 8, 4311-4323.
46. Giannozzi, P.; Baroni, S.; Bonini, N.; Calandra, M.; Car, R.; Cavazzoni, C.; Ceresoli, D.; Chiarotti, G. L.; Cococcioni, M.; Dabo, I.; Dal Corso, A.; de Gironcoli, S.; Fabris, S.; Fratesi, G.;

Gebauer, R.; Gerstmann, U.; Gougoussis, C.; Kokalj, A.; Lazzeri, M.; Martin-Samos, L., *et al.*, Quantum Espresso: A Modular and Open-Source Software Project for Quantum Simulations of Materials. *J. Phys.: Condens. Matter* **2009,** 21, 395502.
47. Standard Solid-State Pseudopotentials (Sssp), Http://Www.Materialscloud.Org/Sssp/. (1/01/2018),
48. Marzari, N.; Vanderbilt, D.; De Vita, A.; Payne, M. C., Thermal Contraction and Disordering of the Al(110) Surface. *Phys. Rev. Lett.* **1999,** 82, 3296-3299.
49. Cooper, V. R., Van Der Waals Density Functional: An Appropriate Exchange Functional. *Phys. Rev. B* **2010,** 81, 161104.
50. Hamada, I.; Otani, M., Comparative Van Der Waals Density-Functional Study of Graphene on Metal Surfaces. *Phys. Rev. B* **2010,** 82, 153412.
51. Lee, K.; Murray, É. D.; Kong, L.; Lundqvist, B. I.; Langreth, D. C., Higher-Accuracy Van Der Waals Density Functional. *Phys. Rev. B* **2010,** 82, 081101.
52. Vydrov, O. A.; Van Voorhis, T., Nonlocal Van Der Waals Density Functional Made Simple. *Phys. Rev. Lett.* **2009,** 103, 063004.
53. Vydrov, O. A.; Van Voorhis, T., Nonlocal Van Der Waals Density Functional: The Simpler the Better. *J. Chem. Phys.* **2010,** 133, 244103.
54. Sabatini, R.; Gorni, T.; de Gironcoli, S., Nonlocal Van Der Waals Density Functional Made Simple and Efficient. *Phys. Rev. B* **2013,** 87, 041108.
55. Deringer, V. L.; Tchougreeff, A. L.; Dronskowski, R., Crystal Orbital Hamilton Population (Cohp) Analysis as Projected from Plane-Wave Basis Sets. *J. Phys. Chem. A* **2011,** 115, 5461-6.
56. Blöchl, P. E., Projector Augmented-Wave Method. *Phys. Rev. B* **1994,** 50, 17953-17979.
57. Golesorkhtabar, R.; Pavone, P.; Spitaler, J.; Puschnig, P.; Draxl, C., Elastic: A Tool for Calculating Second-Order Elastic Constants from First Principles. *Comput. Phys. Commun.* **2013,** 184, 1861-1873.